Numerical study of vapor bubble effect on flow and heat transfer in microchannel

Zhiqiang Dong [a],[*], Jinliang Xu [b], Fangming Jiang [a], Pei Liu [a]

[a] CAS Key Laboratory of Renewable Energy and Gas Hydrate, Guangzhou Institute of Energy Conversion, Chinese Academy of Science, Guangzhou 510640, PR China
[b] Beijing Key Laboratory of New and Renewable Energy, North China Electric Power University, Beijing, 102206, PR China

ABSTRACT

Flow boiling in a microchannel is characterized by nucleation and dynamic behavior of vapor bubbles in the channel. In the present study, the effect of vapor bubble on fluid flow and heat transfer in a micro-channel is investigated via lattice Boltzmann (LB) modeling. With respect to boiling flow in a single microchannel, the bubble nucleation, growth, and departure are simulated by using an improved hybrid LB model. Relating bubble behavior with fluid flow and boiling heat transfer provides some insight into the relevant fundamental physics on flow boiling in the microchannel. It is found that the bubble growth before its departure from the wall induces an obvious resistance to the fluid flow. The processes of nucleation and motion of different bubbles interact, leading to an alternate, either enhanced or weakened, effect of bubble behavior on the flow boiling.

© 2011 Elsevier Masson SAS. All rights reserved.

1. Introduction

Flow boiling in a confined space involves many complex phenomena such as bubble nucleation, growth, departure, and coalescence. In flow boiling systems, different from single phase liquid flow, phase change dominated by heat transfer causes the fluid volume expansion due to density change, yielding the two-phase flow instability. Though many studies on flow instability in microchannels have been reported in recent years, the relevant mechanism is not fully understood yet, especially the relationship of flow boiling instability and bubble dynamical behaviors. Flow instability in microchannels not only causes an uneven thermal stress on the heated surface, but also leads to an early onset of critical heat flux (CHF). Recent studies worldwide on this topic focused on either the description of the flow instability phenomena, or measures to migrate or suppress the flow instability.

The two-phase flow instability was proposed firstly by Ledinggs in 1938 [1]. In 1966, Boure et al. [2] took the instability into categories and analyzed its trigger mechanism. Kandlikar et al. [3] reported the reversed flow induced by the expanding growth of vapor bubble in parallel microchannels of 1 mm hydraulic diameter using high speed video camera in 2001. Qu and Mudawar (2003) [4] have found the interaction of flow instability induced in a flow system of 21 parallel microchannels on the cuprum heat sink. Hetsroni et al. [5] investigated boiling heat transfer in parallel microchannels using water and ethanol as the working fluids. Their experiments

covered data ranges: hydraulic diameter of 100–220 μm, mass flux of 32–200 kg/m^{2}s, heat flux of 120–270 kW/m^2 and vapor mass quality of $x = 0.01$–0.08. The cycle period was dependent on the boiling number and decreased with the increase of boiling number. Dynamic changes of pressure drop, fluid across and temperature at the heated surface were both periodic at a same oscillation frequency. Chang and Pan [6] reported experimental results in a heat sink of 15 parallel microchannels. Flow patterns were found to be significantly different under stable and unstable flow conditions. Bubble nucleation, slug flow and slug or annular flow appeared sequentially along the flow direction for the stable flow, whereas forward or reversed slug/annular flows appeared alternatively in each channel for the unsteady flow. Huh and Kim (2006) [7] found the flow instability still occurred in a single microchannel. Huh et al. [8] studied the flow instability induced by the flow pattern transition in a single microchannel, which was made of polydimethylsiloxane (PDMS) and rectangular with 103.5 μm hydraulic diameter and 40 mm length. Fluid pressures, inlet and outlet fluid temperatures and heated surface temperatures were found to oscillate, matching the alternating flow pattern transitions with time in the microchannel. Qu and Mudawar [9] studied transport phenomena in two-phase microchannel heat sinks. Periodic pressure drop, large amplitude oscillations of inlet and outlet pressures and heat sink temperatures were observed. It is speculated that such kind of flow instability can be mitigated by setting a throttle valve at the microchannel upstream.

Kandilikar et al. (2005) [10] applied the throttle measure at the entrance of microchannel, which enforced water to pass through a smaller aperture into the microchannel, effectively preventing the

* Corresponding author. Tel.: +86 20 87059620; fax: +86 20 87057776.
E-mail address: dongzq@ms.giec.ac.cn (Z. Dong).

Nomenclature

$\mathbf{e}$	velocity vector of LBM
f	distribution function
g	distribution function
h	distribution function
h_{fg}	latent heat of evaporation
H	the equivalent size of channel
Ja	Jacob number
K	thermal diffusivity
n	total number density
Nu_x	$= -(\frac{dT}{dy})_{y=0}/(\frac{\Delta T}{H})$ local Nusselt number at the heated wall
Nu	$= 1 + \frac{\langle u_y T \rangle}{K\Delta T/H}$ average Nusselt number
Pe	Peclet number
t	time
T	temperature
$\mathbf{V}_x$	macroscopic velocity of fluid along x-direction

$\mathbf{x}$	coordinates (X,Y)

Greek symbols

δ	discrete size
θ_M	mobility
ρ	density of fluid
λ	thermal conductivity
Γ	mobility coefficient
ω	assigning parameter
τ	relaxation parameter
Φ	density difference (phase order parameter)
μ_Φ	chemical potential

Subscripts/superscripts

i	discrete number
b	bubble
G/g	Gas
L/l	liquid
eq	equilibrium

reverse flow and suppressing the flow oscillation. Wang et al. [11] studied throttles of different inlet and outlet configurations to suppress the flow instability in microchannels. With different idea about throttle measures, Kuo and Peles [12] mitigated the flow boiling instabilities in microchannels by artificial reentrant cavities. Xu et al. [13,14] proposed the idea using seed bubbles to eradicate the flow boiling instabilities in microchannels. The reentrant cavities increased the flow resistance. Moreover, the flow instability was sensitive to the number of seed bubbles especially in the situation of smaller heat flux. To unravel the relevant mechanisms, the effects of bubble growth on microchannel flow need to be studied.

Many ideas about how to stabilize flow in microchannels were proposed based on the sense of taking vapor bubble growth as the direct reason inducing flow instabilities. Although the corresponding experiments can explain the physical mechanism of bubble growth and bubble behavior qualitatively, it is generally hard to conduct quantitative research work. Fortunately, the development of numerical methods and computer technology provide a powerful tool to predict vapor bubble behavior in microchannel flow boiling.

Mukherjee et al. [15] applied the level-set method to investigate the bubble growth effect on the heat transfer and reverse flow in microchannels. Taha et al. [16] took the VOF method to study the slug bubble in microchannel flow boiling. These two, as representative works, proposed instructive reference for exploring the mechanisms of bubble behavior. Most of these numerical works focused on the exploding growth of bubble in microchannel due to large phase-change heat flux. But in the microchannel bubble flows, bubble behaviors like bubble nucleation, growth, and coalescence with small growth rate still have important influence on flow boiling. These influences should be taken into account for designing measures to suppress the flow instability like Kuo's reentrant cavity [12] and Xu's seed bubble [13,14].

The objective of this paper is to numerically study the bubble dynamical behavior with smaller growth rate and its influence on the fluid flow and heat transfer in microchannel, using an improved hybrid lattice Boltzman model [17,18].

2. The hybrid lattice Boltzmann model (LBM) [17,18]

Combining with a LBM thermal model, Zheng's immiscible LBM multiphase model with a large density ratio is extended to a hybrid LBM model to describe the phase-change process with mass and heat transferring through the interface. Based on the Stefan boundary condition, phase change is considered as the change of phase order parameter and is disposed as a source term of the Cahn−Hilliard(C−H) equation. The change of the interfacial position with the time is obtained as a part of the solution of the hybrid lattice Boltzmann equations.

2.1. Zheng's lattice Boltzmann dynamic model

In the simulation of vapor bubbly flows, the binary model proposed by Zheng et al. [19] is employed to track the dynamic evolution of the flow field. In Zheng's model, there are two independent macroscopic parameters, total number density, $n = (\rho_A - \rho_B)/2$ and number density difference $\phi = (\rho_A - \rho_B)/2$, where ρ_A and ρ_B stand for the density of fluid A and fluid B, respectively. The parameter n is proportional to pressure and approximately constant in the whole flow field. The parameter ϕ becomes positive in the region where $\rho_A > \rho_B$ and negative in the other one, and thus it represents two-phase distribution, which is the same as the definition of the Swift's model [20].

Two sets of discretized distribution functions f_i and g_i are used to assign each site, which are related to the parameters n and ϕ, respectively. The distribution function f_i can be used to model the transportation of mass and momentum, while the distribution function g_i can be employed to track the interface. Thus, the corresponding lattice Boltzmann BKG equation is written as follows,

$$f_i(\mathbf{x} + \mathbf{e}_i\Delta t, t + \Delta t) - f_i(\mathbf{x}, t) = \Omega_i, \text{ with}$$

$$\Omega_i = \frac{1}{\tau_n}\left[f_i(\mathbf{x}, t) - f_i^{eq}(\mathbf{x}, t)\right] + \left(1 - \frac{1}{2\tau_n}\right)\frac{\omega_i}{c_s^2}\left[(\mathbf{e}_i - \mathbf{u}) + \frac{(\mathbf{e}_i \cdot \mathbf{u})}{c_s^2}\mathbf{e}_i\right]\left(\mu_\phi\nabla\phi + \mathbf{F}_b\right)\delta t \tag{1}$$

$$g_i(\mathbf{x} + \mathbf{e}_i\Delta t, t + \Delta t) - g_i(\mathbf{x}, t) = (1 - q)[g_i(\mathbf{x} + \mathbf{e}_i\Delta t, t) - g_i(\mathbf{x}, t)] - \frac{1}{\tau_\phi}\left[g_i(\mathbf{x}, t) - g_i^{eq}(\mathbf{x}, t)\right] \tag{2}$$

where, $\mathbf{x}$ is restricted to sites on the lattice and t is discrete time, τ_n, τ_ϕ is the dimensionless relaxation parameter. The equilibrium

distribution functions to satisfy the conservation laws can be expressed as follows:

$$n = \sum_i f_i^{(eq)} \tag{3}$$

$$\mathbf{u} = \frac{1}{n}\left[\sum_i f_i^{(eq)}\,\mathbf{e}_i + \frac{1}{2}\left(\mu_\phi\nabla\phi + \mathbf{F}_b\right)\right] \tag{4}$$

$$\sum_i f_i^{(eq)} e_{i\alpha}e_{i\beta} = \left(\phi\mu_\phi + c_s^2 n\right)\delta_{\alpha\beta} + nu_\alpha u_\beta \tag{5}$$

$$\sum_i g_i = \sum_i g_i^{(eq)} = \phi \tag{6}$$

$$\sum_i g_i^{(eq)} e_{i\alpha} = \frac{\phi}{q}u_\alpha \quad\text{with}\quad q = \frac{1}{\tau_\phi + 0.5} \tag{7}$$

$$\sum_i g_i^{(eq1)} e_{i\alpha}e_{i\beta} = \Xi_{\alpha\beta} \quad\text{with}\quad \Xi_{\alpha\beta} = \Gamma\mu_\phi\delta_{\alpha\beta} \tag{8}$$

where, $\mathbf{u}$ is the macroscopic velocity of the fluid. The chemical potential is given by:

$$\mu_\phi = A\left(4\phi^3 - 4\phi^{-2}\cdot\phi\right) - K\nabla^2\phi \tag{9}$$

By performing a Chapman–Enskog expansion on Eqs. (1) and (2), the macroscopic equations for n and ϕ in the second order precision can be derived as follows.

$$\frac{\partial n}{\partial t} + \nabla\cdot(n\mathbf{u}) = 0 \tag{10}$$

$$\frac{\partial(n\mathbf{u})}{\partial t} + \nabla\cdot(n\mathbf{u}\mathbf{u}) = -\nabla\left(P + \phi\mu_\phi\right) + \phi\nabla\mu_\phi + \nu\nabla^2(n\mathbf{u}) + \mathbf{F}_b \tag{11}$$

$$\frac{\partial\varphi}{\partial t} + \nabla\cdot(\phi\mathbf{u}) = \theta_M\nabla^2\mu_\phi \tag{12}$$

where $\theta_M = q(\tau_\phi q - 0.5)\delta\Gamma$.

From Eqs. (10)–(12), the correspondent equilibrium distribution functions can be constructed as follows:

$$f_i^{(eq)} = \omega_i A_i + \omega_i n\left(3e_{i\alpha}u_\alpha - \frac{3}{2}u^2 + \frac{9}{2}u_\alpha u_\beta e_{i\alpha}e_{i\beta}\right)\text{ (Based on D2Q9)} \tag{13}$$

where,

$$A_1 = \frac{9}{4}n - \frac{15\left(\phi\mu_\phi + \frac{1}{3}n\right)}{4},$$

$$A_{i(i=2,...,9)} = 3\left(\phi\mu_\phi + \frac{1}{3}n\right),$$

$$\omega_1 = \frac{4}{9},$$

$$\omega_{i(i=2,...,5)} = \frac{1}{9},$$

$$\omega_{i(i=6,......,9)} = \frac{1}{36}.$$

$$g_i^{(eq)} = A_i + B_i\phi + C_i\phi\mathbf{e}_i\cdot\mathbf{u}\text{(Based on D2Q5)}$$

where, $B_1 = 1$, $B_i = 0(i\neq 1)$, $C_i = (1/2q)$, $A_1 = -2\Gamma\mu_\phi$, Γ is the diffusion coefficient.

2.2. Inamuro's thermal LBM model

Inamuro et al. (2002) [21] proposed a model for the diffusion system including heat transfer. In their model, there is the simplest distribution function h_i among other thermal models. The LBM equation can be written as:

$$h_i(\mathbf{x} + \mathbf{e}_i\Delta t, t + \Delta t) - h_i(\mathbf{x}, t) = -\frac{1}{\tau_T}\left[h_i(\mathbf{x}, t) - h_i^{eq}(\mathbf{x}, t)\right], \tag{14}$$

where τ_T is the dimensionless relaxation parameter.

The equilibrium distribution function (based on D2Q9) for the thermal model can be stated as follows:

$$h_i^{eq}(\mathbf{x}, t) = \omega_i T(1 + 3\mathbf{e}_i\cdot\mathbf{u}) \tag{15}$$

where T is the temperature.

The diffusion equation corresponding to the thermal model can be expressed as:

$$\frac{\partial T}{\partial t} + u_\alpha\frac{\partial T}{\partial x_\alpha} = \delta\frac{1}{3}\left(\tau_T - \frac{1}{2}\right)\frac{\partial^2 T}{\partial x_\alpha^2} \tag{16}$$

2.3. Phase change based on assumption of Stefan boundary

In the Landau mean-field theory, the phase change is considered as a continuous variable of order parameter. So, the corresponding Cahn–Hilliard equation can also be extended to include a phase-change term in the non-isothermal system. The phase change can be identified by calculating the change of phase order parameter. Such a treatment can make the interface be automatically traced based on the change of the phase order parameter. At the same time, the corresponding phase-change latent heat is also considered in the LBM model of the reference [21].

In order to simulate the departure of the vapor bubble from a superheated wall and its growth in superheated liquid, the assumptions have to be considered as follows:

(1) The vapor inside the bubble is pure and approximately incompressible;
(2) The heat transferred from the liquid to the interface is completely used to evaporate the liquid at the interface based on the Stefan boundary, which results in the net increase of bubble volume.

A vapor bubble of volume V_b' is introduced into the superheated liquid. In interval from t' to $t' + \Delta t'$, the mass transferring into the bubble during the phase-change process is expressed as:

$$\int_{V'}\frac{\Delta m}{\Delta t'}dV' = \int \rho_G\frac{dV_b'}{dt}\,dV' = -\frac{1}{h_{fg}}\int_{S'}\lambda_l\left(\frac{\partial T'}{\partial x'}\right)_b dS'$$
$$= -\frac{1}{h_{fg}}\int_{V'}\lambda_l\left(\frac{\partial^2 T'}{\partial x'^2}\right)_{V'}dV' \tag{17}$$

where ρ_G is vapor density, T' is temperature, h_{fg} and λ_l are the latent heat of evaporation and the thermal conductivity, respectively.

Based on phase order parameter, the phase-change is taken into account and expressed as:

$$\dot{\phi} = \frac{\Delta\phi}{\Delta t} = \frac{(\rho_L - \Delta m) - (\rho_G + \Delta m)}{2\Delta t'} - \frac{\rho_L - \rho_G}{2\Delta t'} = -\frac{\Delta m}{\Delta t'} \qquad (18)$$

Eq. (17) is normalized by the following equations:

$$V_b = \frac{V'_b}{V'_{bo}}, \ t = \frac{t'U_T}{d_e}, \ T = \frac{T' - T'_\infty}{T'_b - T'_\infty}, \ x = \frac{x'}{d_e},$$

where V'_{bo} is the bubble volume at an initial stage, d_e is the equivalent diameter of the bubble, U_T is terminal rising velocity of the bubble and T'_∞ is the temperature of liquid at the top boundary of the domain. So, the dimensionless form of Eq. (17) is written as:

$$\rho_G \frac{dV}{dt} = -\frac{\lambda_l(T'_b - T'_\infty)}{h_{fg}U_T d_e}\left(\frac{\partial^2 T}{\partial x^2}\right) \qquad (19)$$

By introducing the *Jacob* number $Ja = (1/h_{fg})C_{pl}(T'_b - T'_\infty)$ and the *Peclet* number $Pe = \rho_L U_T d_e C_{pl}/\lambda_l$, the Eq. (19) can be expressed as:

$$\frac{dV}{dt} = -\frac{\rho_L}{\rho_G}\frac{Ja}{Pe}\left(\frac{\partial^2 T}{\partial x^2}\right) = \frac{\dot{\phi}}{\rho_L - \rho_G} \qquad (20)$$

To include the phase change, the LBM Eq. (2) when $\phi < 0$ is rewritten as:

$$g_i(\mathbf{x} + \mathbf{e}_i\Delta t, t + \Delta t) - g_i(\mathbf{x}, t) = (1 - q)[g_i(\mathbf{x} + \mathbf{e}_i\Delta t, t) - g_i(\mathbf{x}, t)]$$
$$- \frac{1}{\tau_\varphi}\left[g_i(\mathbf{x}, t) - g_i^{eq}(\mathbf{x}, t)\right] + \omega_i\dot{\phi} \qquad (21)$$

In the Eq. (16), $\delta(1/3)(\tau_T - (1/2)) = 1/Pe$. So when $\phi < 0$, the latent heat term $(\rho_G/\rho_L(\rho_L - \rho_G))\cdot\dot{\phi}/Ja$ can be added into the LBM Eq. (14):

$$h_i(\mathbf{x} + \mathbf{e}_i\Delta t, t + \Delta t) - h_i(\mathbf{x}, t) = -\frac{1}{\tau_T}\left[h_i(\mathbf{x}, t) - h_i^{eq}(\mathbf{x}, t)\right]$$
$$+ \omega_i\frac{\rho_G}{\rho_L(\rho_L - \rho_G)}\frac{\dot{\phi}}{Ja} \qquad (22)$$

By using the Taylor series expansion and the Chapman–Enskog expansion for Eqs. (21) and (22), the improved governing equations when $\phi < 0$ can be approximately recovered in the second order:

$$\frac{\partial\phi}{\partial t} + \nabla\cdot(\phi u) = \theta_M\nabla^2\mu_\phi - \frac{\rho_L(\rho_L - \rho_G)}{\rho_G}\frac{Ja}{Pe}\left(\frac{\partial^2 T}{\partial x^2}\right) \qquad (23)$$

$$\frac{\partial T}{\partial t} + u_\alpha\frac{\partial T}{\partial x_\alpha} = \delta\frac{1}{3}\left(\tau_T - \frac{1}{2}\right)\frac{\partial^2 T}{\partial x_\alpha^2} - \frac{\rho_G}{\rho_L(\rho_L - \rho_G)}\frac{\dot{\phi}}{Ja} \qquad (24)$$

3. Numerical simulation

3.1. Code validation

Before applying the code to calculate flows with heat and mass transfer in a microchannel, we did a preliminary test. Model predictions were compared to experimental data.

3.2. Experimental

Fig. 1(a) sketches the configuration of a heat sink with a single microchannel (Xu et al. [22]). The microchannel with a width of 0.2 mm, a length of 7.5 mm and a depth of 0.04 mm was enchased on a silicon wafer of 2 mm width, 7.5 mm length and 0.4 mm depth. Using the carbinol as working fluid, the framework of the testing setup is the same as reported in those published literature [13,14], which is not repeated here for the sake of brevity. The liquid mass flux into the microchannel is $Q = 14.0$ ml/h and the wall temperature in this case is $T_w = 66.4$ °C ($T_{sat} = 64.7$ °C).

3.3. Modeling strategy

We simplified the 3D experimental microchannel into 2D with the length and width of the microchannel taken into account. The configuration of the simulated 2D microchannel heat sink is schematically shown in Fig. 1 (b). A constant velocity boundary with initial entrance velocity 0.486 m/s was set at the left boundary and an extrapolated right boundary was assumed. The bottom and top walls are heated. The numerical mesh system has meshes $Z \times X = 30 \times 1125$.

In experiment, the seed bubble was triggered and introduced into the microchannel by the Pt microheater heated by a periodical pulsed electric load. In the simulation, the free moving small bubbles were introduced into the microchannel at the same frequency of the pulsed electric load to mimic the effects of seed bubbles. The dynamics force, surface tension, pressure are the dominant forces, controlling bubble motion and shape deformation.

3.4. Scaling factors

Based on the similarity principle of fluid flow, the LBM dimensionless parameters are evaluated as

$$\rho_L = 749, \ \rho_G = 1.154, \ Re = 107, \ Pe = 1100,$$
$$Ja = 2.64(\Delta T = 1.7°C)$$

The dimensionless time size is defined as $\delta t = 0.167 \times 10^{-4}$ s and the dimensionless space size is defined as $\delta x = 2.0 \times 10^{-4}$ m. The non-dimensional temperature is defined as $T = T' - T_{sat}/T_W - T_{sat}$.

Comparison of the simulated results and experimental data at $T_w = 66.4$ °C is presented in Fig. 2. It can be seen that the model prediction is in good agreement with the experimental observation, though some deviations are evident to see. One possible reason causing these deviations can be the 2D simulations may not fully represent the real 3D situation in experiments. Nevertheless, through the above test case the developed hybrid LB model is
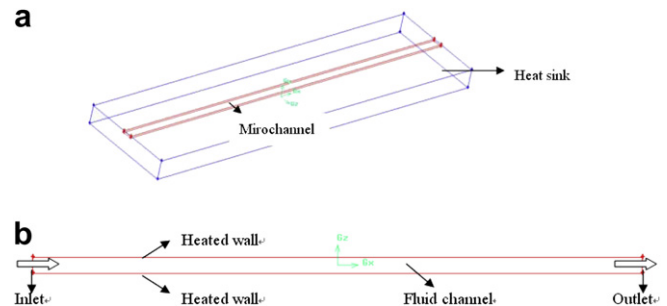

Fig. 1. Single microchannel heat sink (a) The single microchannel heat sink used in the experiment [22]. (b) Configuration of the simulated microchannel of a heat sink.

validated to be able to correctly predict the fluid flow and heat transfer in microchannel heat sink.

3.5. Simulated cases

We performed case studies using the developed LB model. Two dimensional microchannel (0.2 mm × 5.3 mm) is considered. The configuration of the simulated cases is shown in Fig. 3. The bottom boundary is a heated wall of partial wetting surface property. The top boundary is an adiabatic non-wetting boundary. The mesh system has $Y \times X = 50 \times 800$ meshes, where fluid domain contains $Y \times X = 30 \times 800$ meshes, and the bottom wall is resolved with $Y \times X = 20 \times 800$ meshes.

A pressure drop $\Delta p = 0.003$ is imposed along the flow to mimic the effect of minisize pump in reality. The initial velocity of fluid is set at zero. A periodic boundary pair is assumed for the left and right boundaries. Through a series of settings, the minisize pump trigger influences at $t = 0$ in experiment can be also embodied in the simulation. In addition, other initial and boundary condition are kept as the primary setting excluding $Ja = 1.46$ ($\Delta T = 1°$ C). To investigate the influence of bubble behavior on boiling in microchannel, six cases were calculated.

Case1: fluid flow and heat transfer without phase-change in a single microchannel.

Case2: fluid flow and heat transfer with a single seed bubble in a single microchannel.

$Ja = 1.46$ ($\Delta T = 1°$ C) in case2.1 and $Ja = 7.32$ ($\Delta T = 5°$ C) in case2.2.

Case3: fluid flow and heat transfer with a reentrant cavity in a single microchannel.

In case3.1, the bubble starts to nucleate at $t = 0.0$; in case3.2, the bubble starts to nucleate at $t = 10,000$ time steps.

Case4: fluid flow and heat transfer with one seed bubble and a reentrant cavity in the microchannel.

In case4.1, the bubble starts to nucleate and the seed bubble starts to be induced in microchannel at $t = 0.0$; in case4.2, the bubble starts to nucleate and the seed bubble starts to be induced in microchannels at $t = 10,000$ time steps.

Case5: fluid flow and heat transfer with two synchronously-nucleating reentrant cavities in the microchannel.

At $t = 10,000$ time steps when the flow velocity achieves its stability, the bubbles start to nucleate.

Case6: fluid flow and heat transfer with two asynchronously-nucleating reentrant cavities in the microchannel.
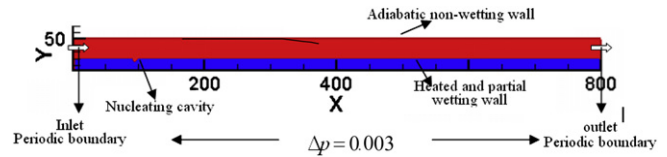

Fig. 2. Comparison of the simulated results and experimental data [22] about bubble growth and motion in the microchannel ($Q = 14.0$ ml/h, $T_w = 66.4$ °C. and $f = 1000/500$ Hz).

Fig. 3. Configuration of the simulated cases.

At $t = 10,000$ time steps when the flow velocity achieves its stability, the first bubble starts to nucleate; at $t = 15,000$ time steps, the second bubble starts to nucleate.

3.6. Effects of single seed bubble

Case1 and Case2 have computed respectively the single phase fluid flow and heat transfer and the multiphase with a single seed bubble flow and heat transfer in microchannel. Fig. 4 shows the single bubble growth and motion in microchannel (time interval = 4000 steps) for case2.2. Comparison between results of case1 and case2 gives information about the influence of seed bubble on the fluid flow and heat transfer in microchannel.

3.6.1. Effects of single seed bubble on fluid flow in microchannel

Effect of the bubble growth rate on the fluid flow is presented in Fig. 5(a). Bubble growth rate directly relates the increasing of bubble size. The smaller the bubble size is, the less its effect is. If the bubble grows sufficiently large, the fluid flow is obstructed and the flow velocity is much affected. This viewpoint can also be confirmed through the fluid speed comparison between experimental results from the cases of seed bubble frequency $f = 500$ Hz and $f = 1000$ Hz (see in Fig. 2). This observation is further analyzed and deduced in Fig. 5(b). In Fig. 5(b), the cross section velocity distribution at different x-position of the microchannel is presented. It shows that the velocity curve at position B presents the parabola profile while the curve at position A has some fluctuation pinnacles. The parabolic velocity profile at position B is an expected result, embodying the influence of solid boundary walls on microchannel flow. Particular attention was paid to explain the shape of velocity profile at position A. This profile represents the typical cross section velocity distribution when the bubble is passing through the position where the velocity is displayed. The fluctuation confirms that the bubble surface tension force strengthens the boundary layer effect and compels the whole bubble to move at lower velocity in the regions close to layer boundary. Because the channel central flow path is blocked by the bubble, the detour flows have been enforced to form in the boundary layers. So the velocity curve at position A has two small protuberances, which locate in the top and bottom boundary layers, respectively. The difference of these two protuberances is a result of the different wetting property of the top and bottom boundary: the bottom is partial wetting boundary while the top non-wetting. From the above analysis, it can be deduced that the bubble surface tension force combines the channel boundary layer to act on the fluid flow in microchannel. Therefore, the measure to reduce the resistance of bubble flow in microchannel needs to combine the effects of surface tension force and boundary layer.
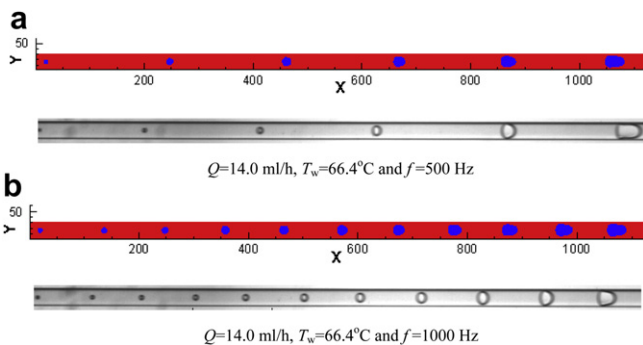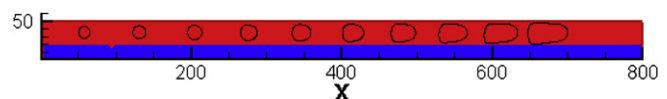

Fig. 4. Single bubble motion in the microchannel ofr Case2.2 (time interval = 4000 steps).
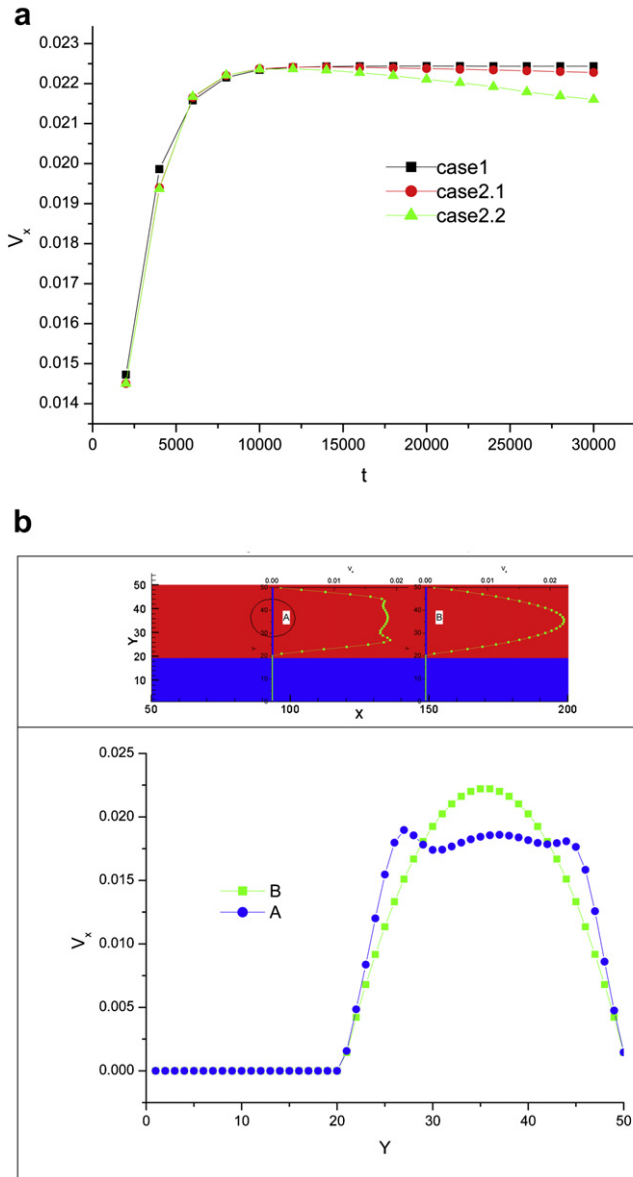
Fig. 5. (a) Effect of seed bubble with different growth rate on fluid flow in the microchannel (note: flow velocity at the center of the channel). (b) Effect of bubble motion on fluid flow in the microchannel (note: the cross section velocity distribution of case2.2).

3.6.2. Effect of single seed bubble on heat transfer in microchannel

The bubble growth effect on the local Nusselt number is presented in Fig. 6(a), which compares the results from cases of different bubble growth rate. At the entrance of microchannel, the local Nusselt number is higher because super-cooling liquid is flowing in. When a single seed bubble flows inside the microchannel, it shows the effect of bubble growth and motion on heat transfer in microchannel. It can be easily seen that larger Nusselt number is present in the entrance region and a protuberance is formed at the curve and floats with bubble motion because the bubble growth consumes the phase-change latent heat at the two-phase interface. That is to say bubble growth caused by the phase-change at two-phase interface enhances the heat transfer around the bubble. The comparison shows that more quickly the bubble is growing, the more phase-change latent heat is consumed and the more evident influence of the bubble growth

on the microchannel heat transfer is. Comparison of the average Nusselt number in fluid field between the single phase flow and the single seed bubble flow is presented in Fig. 6 (b). It can be seen that the efficiency of convectional heat transfer in single phase flow is gradually depressed with time. But the efficiency of convectional heat transfer in seed bubble flow is gradually increased with time. It demonstrates that the bubble disturbance upon flow field can enhance the convectional heat transfer in microchannel. Moreover, more quickly the bubble grows, more intensively the fluid field is disturbed and higher is the heat transfer efficiency.

Fig. 7 shows the disturbance of seed bubble growth and motion to the temperature field of fluid flowing in the microchannel. Because the phase-change occurs at the two-phase interface, the latent heat is also consumed at the bubble interface. The bubble disturbance on temperature field is drifting and changing with the bubble motion and deformation.

3.7. Effect of single nucleating bubble

Case3 and Case4 have simulated the fluid flow and heat transfer when a single reentrant cavity is introduced in the microchannel
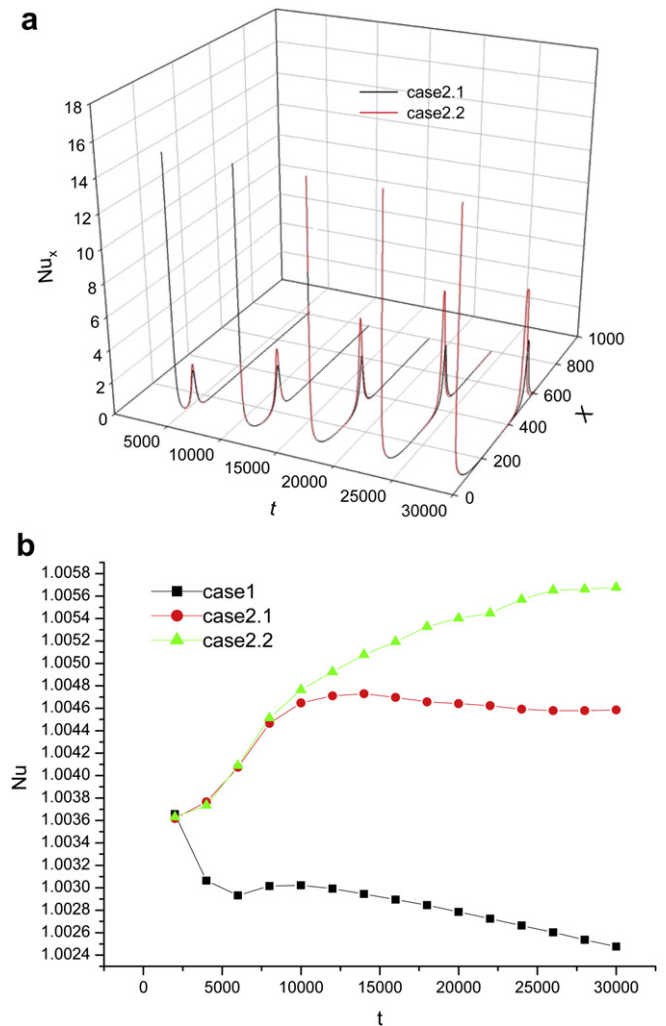

Fig. 6. (a) Comparison of local Nusselt number from cases of different bubble growth rate. (b) Effect of seed bubble growth on convectional heat transfer (average Nusselt number).
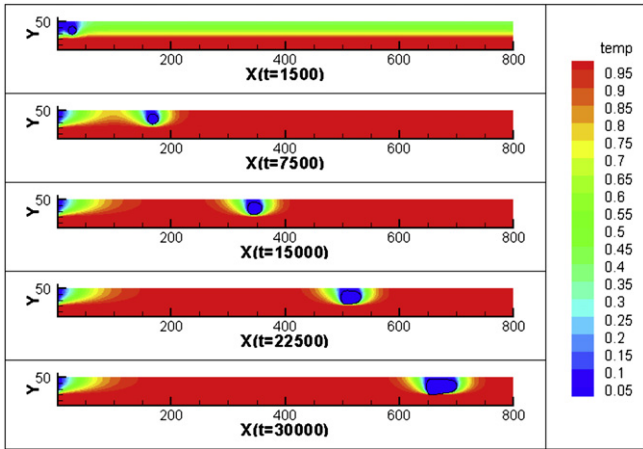
Fig. 7. Effect of seed bubble growth on temperature field evolution (case2.2).

and when both a reentrant cavity and a seed bubble are simultaneously introduced in the microchannel, respectively. Fig. 8(a) displays the result from case3, which presents a free bubble nucleating process (including the bubble growth, departure and motion) due to artificial reentrant cavity. In Fig. 8(b), result from case4 shows the bubble nucleating process is intervened by a seed (motion) bubble. Through the comparison between results from case3 and case4, the effects of the seed bubble and nucleating bubble due to reentrant cavity on fluid flow and heat transfer in microchannel can be revealed.

3.7.1. Effect of nucleating bubble on fluid flow in microchannel

The influence of the bubble nucleation on fluid flow is presented in Fig. 9 (a) and (b). In Fig. 9 (a), the bubble in case3.1 and case4.1 start to nucleate at time $t = 0.0$ step when fluid flow velocity is zero. Due to the pressure gradient existing in the microchannel, the fluid flow velocity experiences an accelerating process to achieve its stable range. In case3.1 and case4.1, this accelerating process is intervened by the bubble nucleation because the bubble growth and expansion before its departure in microchannel bring an obvious flow resistance to the flow. With the completion of the bubble departure, the flow resistance trends to disappear. Moreover, the resistance will be weakened if the nucleating bubble is dragged to depart in advance due to its coalescence with seed bubble as for case4.1. In Fig. 9 (b), the bubble of case3.2 and case4.2 start to nucleate at time $t = 10000.0$ step when fluid flow velocity has achieved its stabilization. The flow resistance will take effect once the bubble nucleation starts. Hence, the
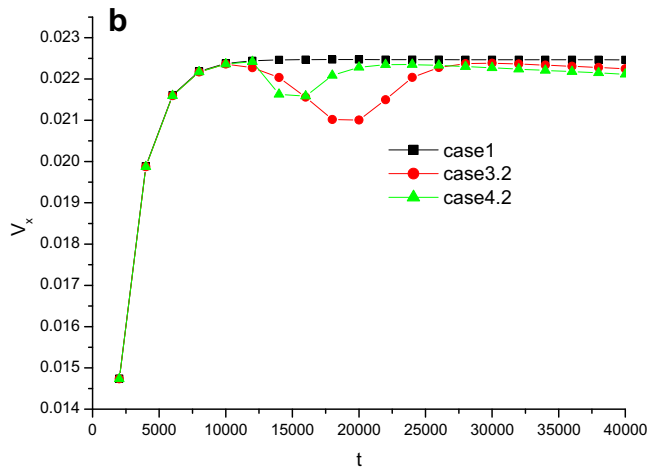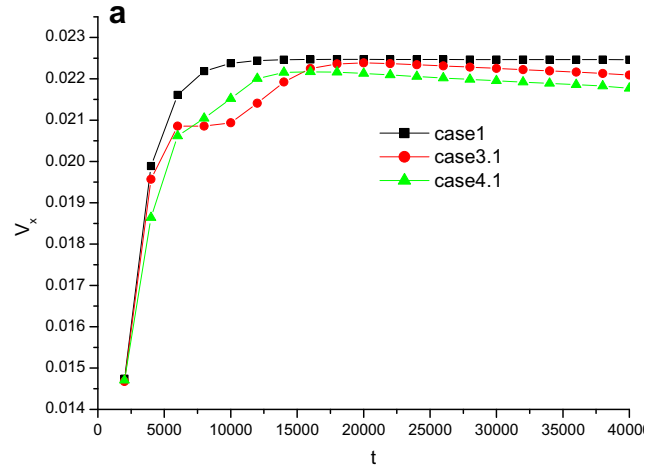

Fig. 8. Bubble growth and departure in the microchannel of case3.1 or case4.1 (time interval = 4000 steps) (a) Nucleating bubble growth and departure on the heated wall (case3.1). (b) Nucleating bubble growth and departure on the heated wall, dragged by seed bubble (case4.1).

Fig. 9. Effect of bubble departure on fluid flow (velocity at channel center).

fluid flow velocity evolution experiences a decrease then increase process within the original stable range. Obviously, the seed bubble weakens the development of this process at the velocity curve as the seed bubble coalesces and drags the nucleating bubble to depart in advance. This can be one of the reasons why the artificial reentrant cavities are not able to completely eliminate flow boiling instability in microchannel. As the seed bubble can coalesce with the nucleating bubble and promote it to depart from the heated wall, adding seed bubbles weakens the resistance of microchannel flows with nucleating bubbles growing on the heated wall to some extent. The disturbance of seed and nucleating bubble on the microchannel flow field of case3.1 and case4.1 are presented in Fig. 10. In Fig. 10 (a), it can be found that the nucleating bubble growth blocks the fluid flow in microchannel. Simultaneously, a high speed region of bypass flow is formed on top of the bubble. This high speed region enlarges with the bubble growth. Furthermore, it starts to disappear while the bubble starts to depart from the heated wall. When the nucleating bubble drifts together with the fluid flow in microchannel, the corresponding bypass flow region completely disappears. In Fig. 10 (b), the coalescence effect of the seed bubble and nucleating bubble on the fluid flow in microchannel is shown. It is seen that the seed bubble combines with the nucleating bubble and drag the nucleating bubble to depart in advance. This process obviously weakens the resistance and restrains the bypass flow region resulted from the nucleating bubble growth.
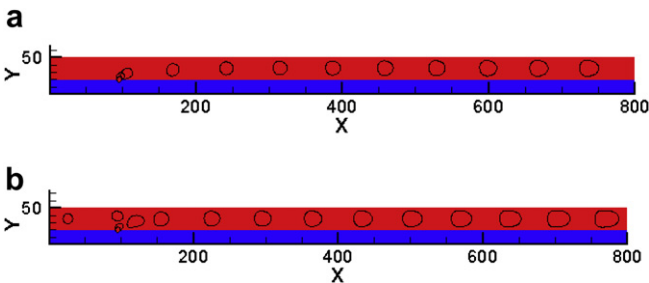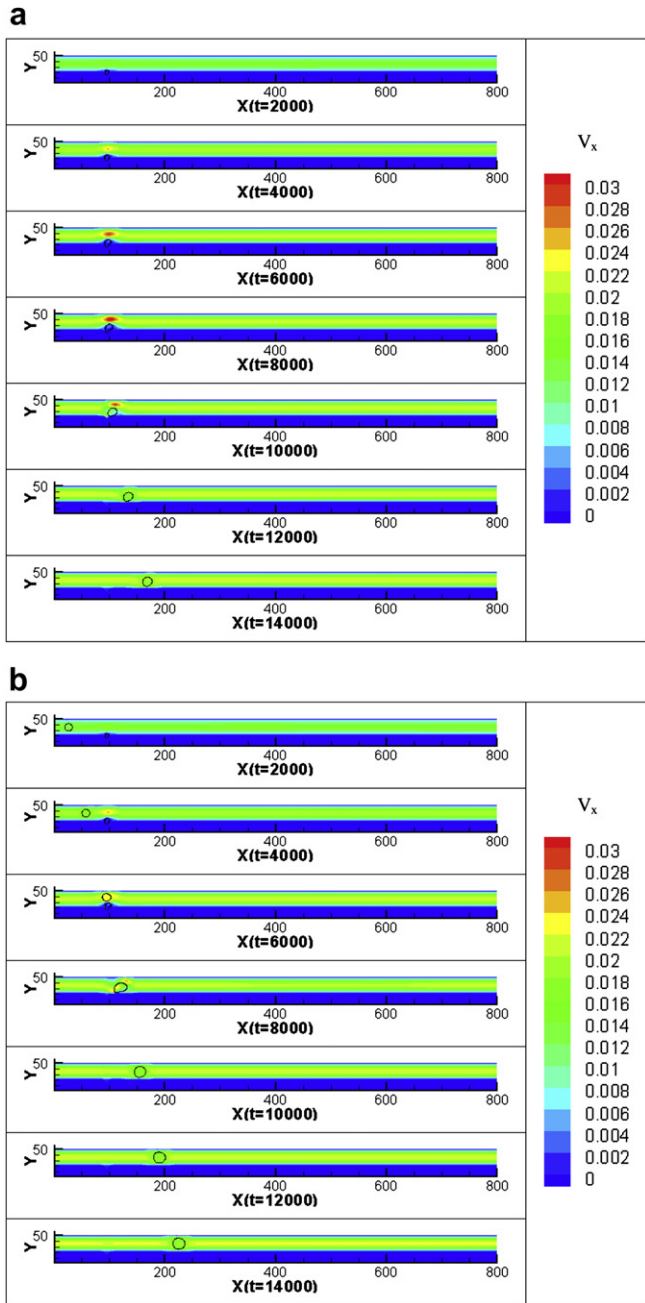
Fig. 10. (a) Effect of the nucleating bubble departure on flow field development (case3.1). (b) Flow field development from the case with nucleating bubble departure dragged by seed bubble (case4.1).

3.7.2. Effect of nucleating bubble growth and departure on heat transfer in microchannel

The influence of bubble growth and departure on the Nusselt number for case3.1 and 4.1 are respectively shown in Fig. 11 (a) and (b). In Fig. 11 (a), It is seen that the nucleating bubble growth before its departure induces a very high local Nusselt number at the position of reentrant cavity. With the bubble departure completed, this highly efficient heat transfer region disappears. Comparison between case3.1 and 4.1 shows that the seed bubble drags the nucleating bubble to depart in advance, lowering the value of local Nusselt number at the reentrant cavity. In Fig. 11 (b), results of average Nusselt number from case3.1 and case4.1 are presented. It can be seen that the bubble growth and

departure induce forced convection around bubble, which enhances locally the heat transfer. The seed bubble can shorten the development process of forced convection through dragging the nucleating bubble to depart from the heated wall in advance. In Fig. 12, the temperature field evolution of case3.1 and 4.1 are presented. It is seen that the disturbance induced by the bubble to the temperature field is drifting with the bubble motion in microchannel.

3.8. Interaction of two nucleating cavities

Case5 and case6 investigate two nucleating bubble effect on fluid flow and heat transfer in microchannel. In case5 the two bubbles are set to nucleate and departure synchronously, while in case6 asynchronously. In case5 the two bubble start to nucleate at the same time $t = 10,000$ steps; in case6 the first bubble starts to nucleate at $t_1 = 10,000$ time steps; the second bubble at $t_2 = 15,000$ time steps. Through these case studies, the influence of two nucleating bubble and their interaction on fluid flow and heat transfer are explored.

3.8.1. Effect of the interaction of two nucleating bubbles on fluid flow in microchannel

Results about the growth, departure and motion of the two synchronously-nucleating bubbles in case5 are shown in Fig. 13.
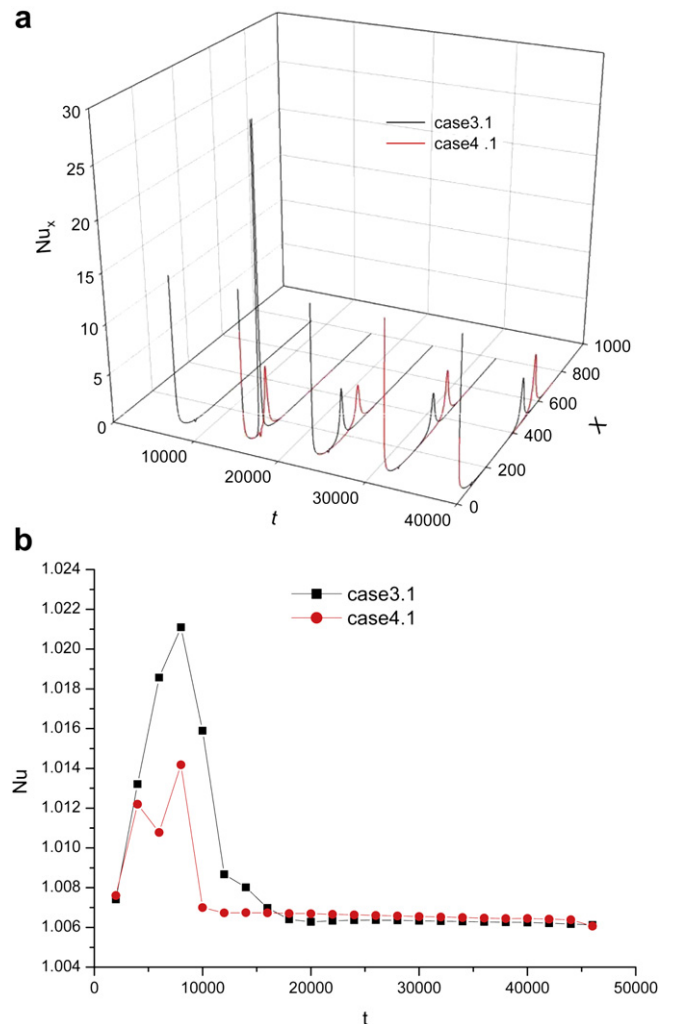

Fig. 11. (a) Local Nusselt number calculated from cases3.1 and 4.1. (b) Average Nusselt number calculated from cases3.1 and 4.1.
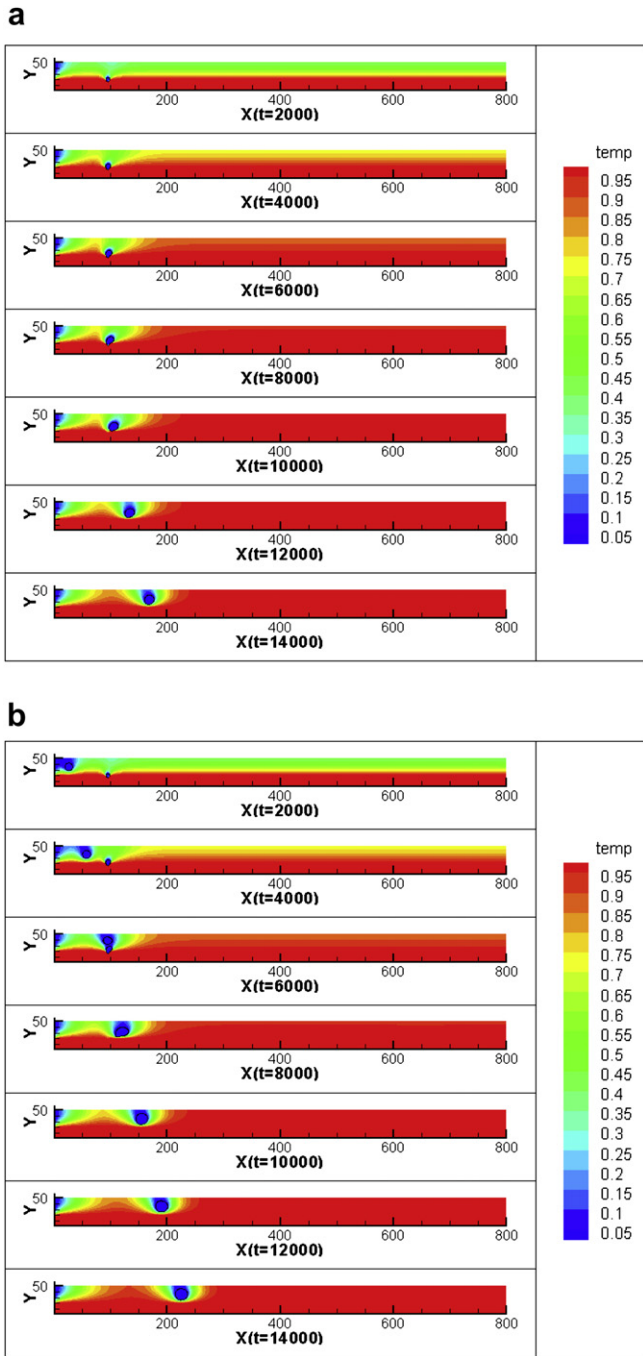
a

b

Fig. 12. (a) Effect of nucleating bubble departure on temperature field evolution (case3.1). (b) Effect of nucleating bubble departure dragged by seed bubble on temperature field evolution (case4.1).

Results about effect of flow resistance induced by bubbles from 4 cases (cases 1, 3.2, 5 and 6) on fluid flow are compared and presented in Fig. 14. Through the comparison with the single phase case, case1 and the multiphase case with single nucleating bubble, case3.2, it is found that the interaction of two synchronously-nucleating bubbles increases the peak resistance, but the interaction process has been not prolonged; in opposition, the asynchronously-nucleating bubbles prolong the interaction process, but the induced peak resistance is less increased. The disturbance of the bubbles on fluid field for case6 is shown in
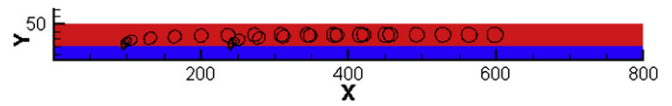

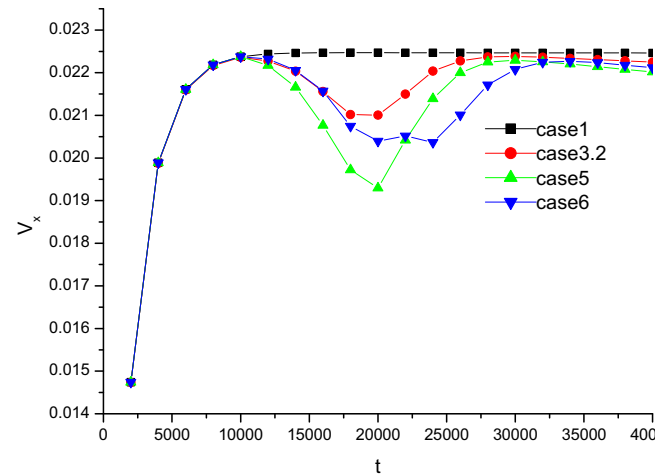Fig. 13. Synchronous departure of two bubbles from case5 (time interval = 4000 steps).

Fig. 14. Velocity (at center of the channel) evolution curves for cases 1, 3.2, 5, and 6.

Fig. 15. It can be seen that the nucleating bubbles interact to emerge an interference and superposition resistance to the flow in the microchannel.

3.8.2. Effect of the interaction of two nucleating bubbles on heat transfer in microchannel

Fig. 16 (a) compares the local Nusselt number of cases 5 and 6, which indicates the bubble growth effect on the heat transfer at microchannel heated wall. The comparison between the calculated average Nusselt number of case5 and case6 is presented in Fig. 16 (b), which is an indication the convectional heat transfer efficiency in the whole microchannel. The bubble departure enhances the convectional heat transfer. The evolution of temperature field for case6 is presented in Fig. 17. It
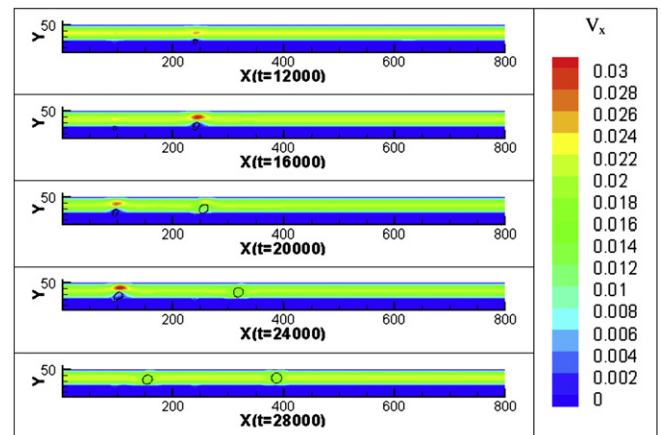

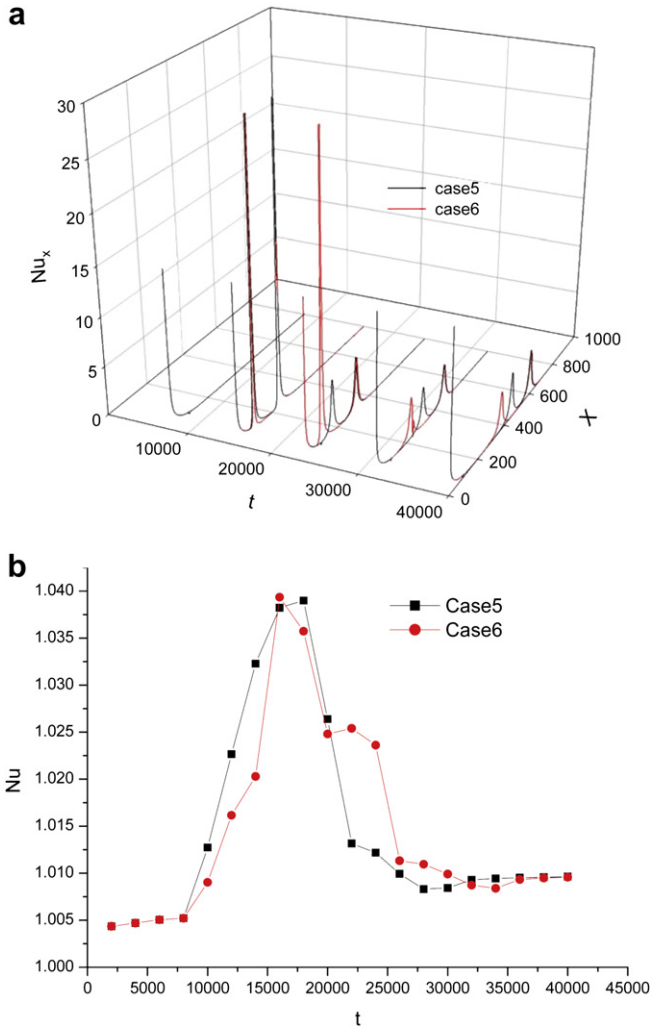Fig. 15. Flow field development from the case with two asynchronously-nucleating bubbles (case6).

Fig. 16. (a) Comparison of the local Nusselt number calculated from case5 and case6. (b) Comparison of the average Nusselt number calculated from case5 and case6.

shows the bubble nucleation, growth and departure disturbs the development of temperature field in the microchannel. All these can be ascribed to the interference and superposition interaction of the two asynchronously-nucleating bubbles.
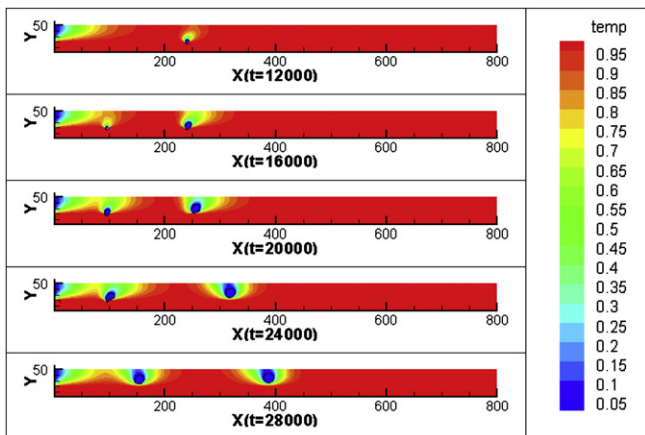

Fig. 17. The evolution of temperature field for the case with two asynchronously-nucleating bubbles (case6).

4. Conclusions

The present work indicates that the developed hybrid LB model is a suitable tool for simulating the flow behavior and heat transfer performance in microchannels. The obtained numerical results shed light on the bubble dynamics, such as the influence of bubble growth and departure on flow disturbance. Major conclusions can be drawn as follows:

1. The bubble growth depresses the fluid flow development in the microchannel. The induced flow resistance increases with the growth of vapor bubble.
2. The consumption of phase-change latent heat enhances heat transfer around the bubble. The enhanced effect drifts with the bubble motion.
3. The growth of nucleating bubble before departure somehow blocks the fluid flow in the microchannel. This blocking effect increases with the bubble growth and disappears with the bubble departure.
4. The nucleating bubble coalesces with the moving bubble and is then dragged to depart prematurely. This can restrain the instability of fluid flow and weaken the singularly high efficiency of heat transfer induced by the bubble nucleation in microchannel to some extent.
5. The bubbles forming at different nucleating cavities induce an interference and superposition resistance on fluid flow in the microchannel.

Acknowledgments

References

[1] M. Ledinggs, Instability of flow during natural and forced circulation, Waerme 61 (8) (1938) 891−898.
[2] J.A. Boure, The Oscillator Behavior of Heated Channels, Part I and II French report CEA-R3049, Grenoble (1966).
[3] S.G. Kandlikar, M.E. Steinke, S. Tian, L.A. Campbell, High Speed Photographic Observation of Flow Water in Parallel Minichannels, ASME National Heat Transfer Conference, Los Angeles, CA, June 10−12, 2001.
[4] W.L. Qu, I. Mudawar, Measurement and prediction of pressure drop in two-phase micro-channel heat sinks, Int. J. Heat Mass Transfer 46 (2003) 2737−2753.
[5] G. Hetsroni, A. Mosyak, E. Pogrebnyak, Z. Segal, Explosive boiling of water in parallel microchannels, Int. J. Multiphase Flow 31 (2005) 371−392.
[6] K.H. Chang, C. Pan, Two phase flow instability for boiling in a microchannel heat sink, Int. J. Heat Mass Transfer 50 (2007) 2078−2088.
[7] C. Huh, M.H. Kim, An experimental investigation of flow boiling in an asymmetrically heated rectangular microchannel, Exp. Therm. Fluid Sci. 30 (2006) 775−784.
[8] C. Huh, J. Kim, M.H. Kim, Flow pattern transition instability during flow boiling in a single microchannels, Int. J. Heat Mass Transfer 50 (2007) 1049−1060.
[9] W.L. Qu, I. Mudawar, Transport phenomena in two-phase microchannel heat sinks, J. Electronic Packaging ASME 126 (2004) 213−224.
[10] S.G. Kandlikar, D.A. Willisern, J. Borrelli, Experimental evaluation of pressure drop elements and fabricated nucleation sites for stabilizing flow boiling in minichannels and microchannels, in: Proceedings of ASME 3rd International Conference on Microchannels and Minichannels, ICMM2005−75197, Toronto, Ontario, Canada (2005).
[11] G.D. Wang, P. Cheng, A.E. Bergles, Effects of inlet/outlet configuration on flow boiling instability in parallel microchannels, Int. J. Heat Mass Transfer 51 (2008) 2267−2281.
[12] C.J. Kuo, Y. Pelses, Flow boiling instabilities in microchannels and means for mitigation by reentrant cavities, J. Heat Transfer 130 (2008). doi:10.1115/1.2908431.
[13] J. Xu, G. Liu, W. Zhang, et al., Seed bubble stabilize flow and heat transfer in parallel microchannels, Int. J. Multiphse Flow 35 (2009) 773−779.
[14] G. Liu, J. Xu, Y. Yang, Seed bubble trigger boling transfer in silicon microchannels, Microfluid Nanofluid 8 (3) (2010) 341−359.
[15] A. Mukherjee, S.G. Kandlikar, Numerical simulation of growth of a vapor bubble during flow boiling of water in a microchannel, Microfluid Nanofluid 1 (2005) 137−145.

[16] T. Taha, Z.F. Cui, CFD modeling of slug flow inside square capillaries, Chem. Engineer. Sci. 61 (2) (2006) 665–675.

[17] Z. Dong, W. Li, Y. Song, Lattice Boltzmann simulation of growth and deformation for a rising vapor bubble through superheated liquid, Numer. Heat Transfer. Part A 55 (2009) 381–400.

[18] Z. Dong, W. Li, Y. Song, A numerical investigation on characteristics of bubble growth on and departure from a superheated wall by using lattice Boltzmann method, Int. J. Heat Mass Transfer 53 (2010) 4908–4916.

[19] H.W. Zheng, C. Shu, Y.T. Chew, A lattice Boltzmann for multiphase flows with large density ratio [J], J. Comput. Phys. 218 (2006) 353–371.

[20] M.R. Swift, W.R. Osborn, J.M. Yeomeans, Lattice Boltzmann simulation of non-ideal fluids [J], Phys. Rev. Lett. 75 (1995) 830–833.

[21] T. Inamuro, M. Yoshino, H. Inoue, R. . Mizuno, F. Ogino, A Lattice Boltzmann method for a binary miscible fluid mixture and its application to a heat-transfer problem, J. Comp. Phys. 179 (2002) 201–215.

[22] J. Xu, W. Zhang, G. Liu, Seed bubble guided heat transfer in a single micro-channel, Heat Transfer Eng. 32 (11–12) (2011) 1031–1036.